applied optics

Fourier transform acousto-optic imaging with off-axis holographic detection

Louis Dutheil,[1] Maïmouna Bocoum,[1] Mathias Fink,[1] Sébastien M. Popoff,[1] François Ramaz,[1] and Jean-Michel Tualle[2,*]

[1]*ESPCI Paris, PSL University, CNRS, Institut Langevin, 1 rue Jussieu, 75005 Paris, France*
[2]*Laboratoire de Physique des Lasers, CNRS, Université Sorbonne Paris Nord, 99 avenue J.-B. Clément, 93430 Villetaneuse, France*
Corresponding author: tualle@univ-paris13.fr

Acousto-optic (AO) imaging is an in-depth optical imaging technique of highly scattering media. One challenging end-application for this technique is to perform imaging of living biological tissues. Indeed, because it relies on coherent illumination, AO imaging is sensitive to speckle decorrelation occurring on the millisecond time scale. Camera-based detections are well suited for *in vivo* imaging provided their integration time is lower than those decorrelation time scales. We present Fourier transform acousto-optic imaging combined with off-axis holography, which relies on plane waves and long-duration pulses. We demonstrate, for the first time to the best of our knowledge, a two-dimensional imaging system fully compatible with *in vivo* imaging prerequisites. The method is validated experimentally by performing in-depth imaging inside a multiple scattering sample. © 2021 Optical Society of America

1. INTRODUCTION

Imaging biological tissues at large depths is a challenge inherent to multiple medical applications such as early tumor detection. Indeed, after a few millimeters of propagation, predominance of the multiple scattering regime is detrimental to optical imaging relying on ballistic light in the visible to near-infrared range [1]. Optical coherence tomography [2,3] is, for instance, limited to about 100 µm in depth, even when standard wavefront correction [4] is used to compensate for strong aberrations. As a way around, diffuse optical tomography [5] has emerged to infer millimeter-to-centimeter depth optical properties of the medium, based on prior knowledge about scattering properties of the medium [6,7].

In this context, photoacoustic imaging (PAI) [8–12] and acousto-optic imaging (AOI) [13,14] have drawn increasing interest over the past decades. They both provide a direct mapping of optical absorption properties of scattering tissues. In PAI, an intense Q-switched nanosecond laser beam is used to heat optical absorbers inside the medium. As they undergo thermal relaxation, those absorbers emit ultrasound (US) waves in the megahertz range, which are detected to reconstruct an optically contrasted image. In AOI, the medium is illuminated with a laser of high temporal coherence, while insonified with an auxiliary US pulse in the megahertz range. As a result of the AO effect [15], the spectrum of light propagating through the insonified region shows two sidebands, which are both shifted from the optical carrier by the US frequency. Those so-called tagged photons, which leave the medium, are then selectively detected. Due to the local character of the tagging, the absorption properties of the medium can be monitored during US ballistic propagation. Up until now, the development of PAI has been faster than that of AOI, as it relies on incoherent illumination. In fact, for clinical applications, coherent illumination is challenging because of the speckle decorrelation caused by Brownian motion of scatterers, blood circulation, and breathing. This decorrelation occurs on time scales in the order or below the millisecond range [16–19]. In the case of AOI, this sensitivity is highly dependent on the technique used to detect the tagged photons. In addition, because only a few percent of the light is tagged by the US, weak signal-to-noise ratio (SNR) is another major challenge to address before considering *in vivo* applications.

The most basic scheme to perform AOI is to use temporally pulsed spatially focused US for insonification. Using a detection fast enough to follow US pulse propagation, a direct space-to-time mapping allows to reconstruct an in-depth image. Fast detection is, for instance, performed using photorefractive holography [20] or spectral hole burning [14,21], both relying on a high-sampling-rate photodiode. Robustness against speckle decorrelation makes spectral hole burning promising, but these systems require cryogenic equipment and are not tunable in wavelength.

Camera-based detection [22] of tagged light is an alternative to those detections, provided the camera integration time remains lower than that of speckle decorrelation. In the particular case of off-axis holography [23], the US frequency-shifted

light interferes on the camera with a reference beam of the same frequency. This gives rise to spatial fringes on the detector with a spacing dependent upon the off-axis angle between the two beams. By digitally processing this signal [24,25], we can retrieve the total number of tagged photons recorded during the camera exposure. Since the camera frames rate (<kilohertz) is orders of magnitude lower than the sampling rate of a fast photodiode (megahertz), it is no longer possible to resolve the propagation of the US pulse, which typically progresses at 1.5 mm μs^{-1}. Furthermore, to maximize the number of tagged photons recorded during one camera exposure, temporally long unfocused US pulses appear a natural choice because they maximize the insonification volume within the sample. The problem arising with such US wave is a complete loss in spatial resolution, since tagged photons now come from the entire insonification plane.

The problem of recovering spatial resolution using plane and/or continuous wave has been extensively reported in the literature [26,27]. In the temporal (i.e., axial) direction, one solution is to increase the spectral bandwidth of the tagging US, and thereby, that of tagged light. This is achieved, for instance, by imposing a frequency chirp [28], or random phase jumps [29] on the US carrier frequency. Imposing the same phase modulation on the reference beam when performing off-axis holography, interferences on the camera only build up when the relative delay between the two beams does not exceed the temporal coherence of these modulations. As a result, the tagged photons seem to be emanating from a confined volume along the US propagation axis, yielding a recovery of axial resolution. The volume of tagged light, however, reduces as we increase the spectral bandwidth, which ultimately also degrades the SNR.

To maximize the tagging volume and maintain spatial resolution, Fourier transform acousto-optic imaging (FT-AOI) was first introduced using spatially focused US [30,31]. There, a long US pulse is periodically modulated either in amplitude or phase. When the same modulation is reproduced on the reference arm, tagged photons appear as if generated by several static points periodically distributed along the direction of propagation. Consequently, one acquisition gives access to one component of the image Fourier transform. In a recent article [32], we have shown that by using a transducer array, the same idea could be extended to fetch the two-dimensional Fourier components of the image. However, this work relied on photorefractive-based holographic detection, and therefore is sensitive to speckle decorrelation. In this paper, we present, for the first time to our knowledge, FT-AOI combined with off-axis heterodyne holographic detection.

2. THEORY

The theoretical framework of the method is described in [30]. The present section focuses on true implementation of the method using a transducer array [32]. In FT-AOI, the pressure field is periodically structured along the x and z axis, corresponding, respectively, to the direction along the transducer array and the direction of acoustic propagation. Reconstructing an image requires performing multiple acquisitions so as to fetch all of its Fourier components. For each acquisition, the structuring frequencies ν_x along the x axis is an increasing harmonic of

fundamental frequencies $\nu_x^0 = L^{-1}$, where L is the width of the US probe, such that $\nu_x = m\nu_x^0$ with m integer. The modulation along z is done by imposing a periodic temporal emission on each transducer with a relative phase imposed by the periodicity set along x. At any given time during propagation, the field thereby appears spatially modulated along z at a frequency $\nu_z = n\nu_z^0$, where n is an integer corresponding to the harmonic order and ν_z^0 is the fundamental modulation frequency. By definition, we have that $\nu_z^0 = (c_s T_0)^{-1}$ with T_0 the user-defined fundamental temporal period and c_s the sound velocity inside the medium. In addition, by controlling the emission time on all transducers simultaneously, we can vary the relative phase ϕ of the structuring pattern. We note $P_{m,n}^\phi(x, t)$ as the pressure field emitted by the transducer array for the (m, n)-harmonic pattern and a phase ϕ at $z = 0$ and for $0 \leq x \leq L$,

$$P_{m,n}^\phi(x, t) = P_0 h_{m,n}^\phi(t, x) \cos \omega_{us} t, \tag{1}$$

where $h_{m,n}^\phi$ stands for the adimensional amplitude of the modulation and P_0 for the nominal pressure. At each position x, $h_{m,n}^\phi(\bullet, x)$ is a T_0/n-periodic function. On one period, it equals to 1 when $0 \leq t < T_0/2n$ and 0 otherwise, such that $(h_{m,n}^\phi)^2 = h_{m,n}^\phi$. By construction, we also impose that function $h_{m,n}^\phi(t, \bullet)$ be L/m periodic along x. This function is represented in Fig. 1 for different values of n, m, and ϕ. By neglecting diffraction effects upon propagation, the pressure field at time t following the emission writes

$$P_{m,n}^\phi(x, z, t) \equiv A_{m,n}^\phi(x, z, t) \cos \left[\omega_{us}(t - c_s^{-1} z) \right], \tag{2}$$

$$A_{m,n}^\phi(x, z, t) = P_0 h_{m,n}^\phi(t - c_s^{-1} z, x), \tag{3}$$

with ω_{us} the US carrier pulsation and P_0 the nominal pressure. As US propagates, some photons are frequency-shifted from the incident optical carrier ω_L at $\omega_L \pm \omega_{us}$ with a phase and amplitude inherited from $A_{m,n}^\phi$. In the holographic digital detection scheme, the collected field E interferes with a reference field $E_{ref\,n}$ centered at $\omega_L + \omega_{us}$. The resulting image $I_{m,n}^\phi(\eta, \xi)$ obtained over an integration time τ_e writes

$$I_{m,n}^\phi(\eta, \xi) = \epsilon_0 \int_{\tau_e} dt |E_{ref\,n}(\eta, \xi, t) + E(\eta, \xi, t)|^2, \tag{4}$$

where (η, ξ) are the pixel coordinates on the camera sensor. By imposing that $E_{ref\,n}$ also be T_0/n periodic in amplitude, constructive interference over the integration time τ_e will only build up for tagged light coming from specific locations in the interaction plane. These locations are defined by our so-called "tagging function." The temporal expression of the reference field incident on the camera writes

$$E_{ref\,n}(\eta, \xi, t) = E_0 \sin^2 \left(\pi \frac{n}{T_0} t \right) e^{-i \frac{\omega_L + \omega_{us}}{c} (\alpha_\eta \eta + \alpha_\xi \xi)} e^{i(\omega_L + \omega_{us})t}, \tag{5}$$

where c is the velocity of light, E_0 is the field amplitude, and α_η and α_ξ the off-axis angles.

Following the basic principle of off-axis holography, the recorded image is numerically filtered in the Fourier domain so as to only keep the tilted component. This operation leads to the following hologram resulting from the interferences between the scattered light and the reference beam:
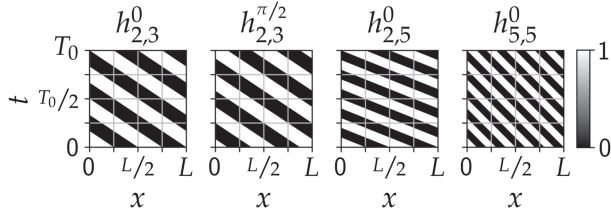
Fig. 1. Examples of the amplitude of modulation $h_{m,n}^{\phi}$.

$$H_{m,n}^{\phi}(\eta, \xi) = \epsilon_0 e^{i\frac{\omega_L + \omega_{us}}{c}(\alpha_\eta \eta + \alpha_\xi \xi)} \int_{\tau_e} dt\, E_0^*(\eta, \xi, t)$$

$$\times \sin^2\left(2\pi \frac{n}{T_0} t\right) e^{-i(\omega_L + \omega_{us})t}. \tag{6}$$

The averaged square modulus of this hologram on all of the pixels, $s_{m,n}^{\phi} \equiv \langle |H_{m,n}^{\phi}|^2 \rangle$, is proportional to the average intensity of the tagged photons selectively detected in the US interaction plane [30]. We write it in the following form:

$$s_{m,n}^{\phi} \propto \int_{x,z} dx\,dz\, I(x, z)\left[M_{m,n}^{\phi}(x, z)\right]^2, \tag{7}$$

where $I(x, z)$ is the image we wish to reconstruct, which depends on the local average intensity of the diffuse light, on the tagging efficiency, and on the propagation from the medium to the camera [30]. $M_{m,n}^{\phi}(x, z)$ is the tagging function that ensures spatial selectivity. As illustrated in Fig. 2, the acoustic field modulation pattern has an arrival phase that varies along x and z. As a result, tagged photons will only be fully correlated with the reference wave at specific positions (x, z). The expression of tagged photons is easily derived from Eq. (2), such that the tagging function becomes the following cross correlation [30]:

$$M_{m,n}^{\phi}(x, z) = \frac{P_0}{\tau_e} \int_{\tau_e} dt \sin^2\left(2\pi \frac{n}{T_0} t\right) h_{m,n}^{\phi}(t - c_s^{-1}z, x)$$

$$= \frac{P_0}{2}\left[1 + \frac{1}{\pi}\cos\left(2\pi m v_x^0 x + 2\pi n v_z^0 z + \phi\right)\right]. \tag{8}$$

Detailed derivation of Eq. (8) is performed in Supplement 1. This expression shows that the sinusoidal modulation applied on the reference beam leads to periodically distributed tagged photons both in the x and z axis. By combining measurements obtained using four different phase shifts, namely, $\phi \in \{0, \pi/2, \pi, 3\pi/2\}$, we access the complex Fourier components $\tilde{I}$ of the acousto-optic image,

$$s_{m,n}^{3\pi/2} - s_{m,n}^{\pi/2} + i\left(s_{m,n}^{\pi} - s_{m,n}^{0}\right) \propto \tilde{I}(m v_x^0, n v_z^0). \tag{9}$$

Image $I(x, z)$ is thus simply reconstructed by performing an inverse Fourier transform (iFT) of $\tilde{I}$. In our model, we, however, recall that diffraction is neglected (Eqs. 2 and 8), a hypothesis that might not always verify experimentally. Thus, to investigate the potential effect of diffraction, we have performed a simulation of the actual pressure emitted by the probe we used in our later described experiment. Simulations were performed using Field II open-source software as already described in [33].
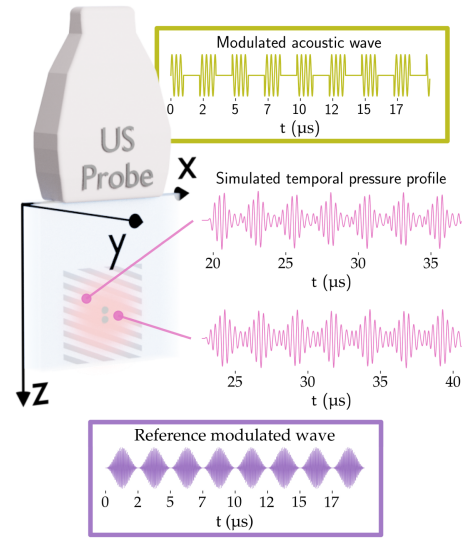

Fig. 2. Principle of the method. The two-dimensional probe sends a temporally modulated acoustic beam (top caption) specified by $h_{m,n}^{\phi}$. The acoustic field that propagates inside the scattering medium is represented at two different arbitrary positions inside the sample. The tagging function will result in the cross correlation of this local field with the reference wave (lower caption).
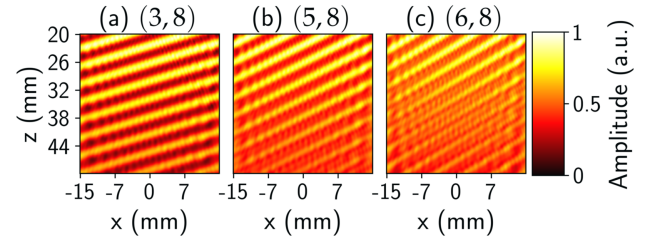

Fig. 3. Simulated tagging functions for (a) $m = 3$, (b) 5, and (c) 6; $n = 8$ on a $20 \leq z \leq 50$ and $-15 \leq x \leq 15$ simulation grid.

A simulation grid is placed in the US plane, 35 mm below the probe emission surface with $-15 \leq x \leq 15$ and $20 \leq z \leq 50$. On each point of a simulation grid, we have calculated the tagging function using the simulated pressure and the expression of our theoretical optical reference field. As a result, we conclude that diffraction effects can indeed be neglected for all n (tested up to 20). As the m value increases, however, second-harmonic artifacts start to appear in the tagging function, together with π-phase shifts of the sin wave. This effect is to be expected as a result of the Talbot near-field diffraction effect and will be fully explained in future work. An example of resulting $M_{m,n}^{\phi}$ functions are shown in Fig. 3 for $m = 3, 5, 6$, and $n = 8$. In our simulated experimental conditions, diffraction artifacts start to appear typically for $|m| \geq 6$, with a noticeable phase shift at ~ 38 mm. For this reason, we constrained our experiment to $|m| < 6$ so as to remain with the scope of validity of our model.

3. EXPERIMENT

The sample is an hydrogel mimicking both the optical and mechanical properties of soft biological tissues [34]. The dimensions of the hydrogel along the x, y, and z axes are, respectively, $5 \times 1 \times 5$ cm^3. The 50 kPa Young modulus is set by
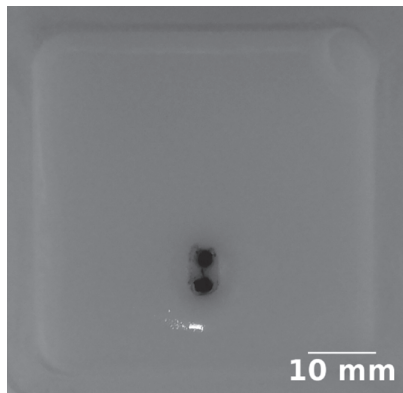
Fig. 4. Photograph of the two ink inclusions taken above the gel cast. The two inclusions stand at 35 mm from the top surface of the gel. This distance corresponds to the elevation focus of the probe.
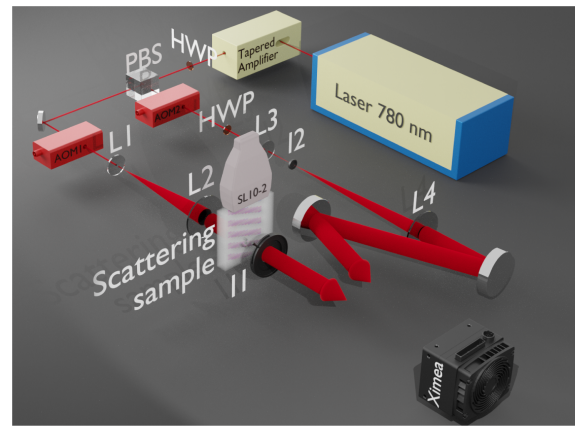

Fig. 5. Experimental setup. Light emitted by a laser diode at 780 nm is split between the probe beam and the reference arm with a half-wave plate (HWP) followed by a polarizing beam-splitter (PBS). Both arms are then modulated in frequency by two acousto-optic modulators (AOM#) around 80 MHz with a relative difference of 3 MHz, corresponding to the carrier frequency of the acoustic waves emitted by the transducer array (SL10-2–Aixplorer SL10-2 US probe, SuperSonic Imagine, Aix-en-Provence, France) through the scattering hydrogel. Lenses (L#) and irises (I#) widen and filter the beams before they meet the camera (Ximea) sensor.

the 2% concentration of agar [35], whereas the concentration of Intralipid 10% is adjusted to obtain a reduced scattering coefficient $\mu'_s = 1$ cm^{-1} (transport mean free path $l^* = 1$ cm) [36]. Two ink inclusions are inserted at a 5 mm depth. The dimensions of their cylindrical shapes are 4 mm in height and 2 mm in diameter. Their centers are separated by 4 mm. A photograph showing the two inclusions taken during the molding is shown in Fig. 4. The sample is illuminated with a single-longitudinal mode laser centered at 780 nm. After the tapered amplifier (MOPA, Sacher Lasertechnik GmBH), the incident power is about 370 mW for a beam diameter of 13 mm. A transmitted photons flux of 3.6 µW is collected by the CMOS camera (Ximea xiB-64) located 34 cm behind the sample output surface. This distance corresponds to a trade-off between proper sampling of the interference fringes and a maximization of the optical collection. A scheme of the experimental setup is presented in Fig. 5.

The structured US plane waves are emitted with a 192-element linear transducer array (Aixplorer SL10-2 US probe, SuperSonic Imagine, Aix-en-Provence, France) with a fixed focal elevation of 35 mm. The excitation voltage of the transducer is set to 15 V such that the nominal pressure of the US wave was measured to be $P_0 \approx 300$ kPa. Such a pressure corresponds to a US peak intensity of ≈ 3 W cm^{-2}. Accounting for the acquisition repetition rate, the average acoustic intensity is ≈ 150 mW cm^{-2}, far below biomedical norms of 720 mW cm^{-2} [37]. We set the fundamental temporal window of our periodic pattern to $T_0 = 20$ µs. The pattern is then repeated 5 times so as to match the exposure time of the camera $\tau_e = 100$ µs. The camera is triggered at a 300 Hz repetition rate, and each component (given n, m, ϕ value) is measured with a single-shot image. Here, we only use a 1024×1024 pixel area of the 16 Mpixel chip, to prevent frame dropping, which occurs when our frame grabber gets filled up. In fact, our image processing performed using LabVIEW software runs on a multicore CPU unit but remains too slow to prevent this buffer saturation at full chip capacity. A full frame acquisition would improve the SNR as the sensor surface is increased but would require a graphics processing unit (GPU) for the reconstruction process. The total acquisition time to image a complete field of view of 30×30 mm^2 is 1.5 s.

We image the two ink inclusions hidden within hydrogels of two different reduced scattering coefficients, 1 and 10 cm^{-1}. The image corresponding to the $\mu'_s = 1$ cm^{-1} hydrogel featured in Fig. 6 shows two dark spots in the halo of the tagged beam. with a diameter of 2 mm, and separated by 4 mm, as expected. This image was reconstructed from the 110 complex Fourier components, $m \in [[-5, 5]]$, $n \in [[1, 10]]$, which modulus is shown in Fig. 6(c). The resolution of FT-AOI is given by the spatial period of the higher harmonics used in the structuring pattern $h_{m,n}$, with the wavelength of the US carrier as the ultimate limit. As the maximum values for m and n are, respectively, $m = 5$ and $n = 10$, the resolutions along x and z are, respectively, $(m\nu_x^0)^{-1} = 7.7$ mm and $(n\nu_z^0)^{-1} = 3$ mm, which discriminates our two inclusions.

To outline the time-efficiency of FT-AOI, we draw a comparison with AO imaging in real space as, for instance, performed using spatially focused US with random phase jumps modulation [22,29]. In this respect, let us assume such an image be sampled every ∼2 mm over a 30×30 mm^2 field of view. This corresponds to $15 \times 15 = 225$ points to acquire. For each sampled point, the AO detected signal in experimental conditions similar to the present work is nearly 1 to 2 orders of magnitude lower [22] than for FT-AOI. In fact, because the tagging volume is reduced to a few cubic millimeters, it requires a proportional increase in the number of averaging. As a result, the acquisition time for an image acquired in real space is on the order of a minute. In FT-AOI, where acquisition is performed in reciprocal space, the tagging volume is significantly increased such that averaging is no longer required. As a result, the method is typically 1 order of magnitude more time-efficient.

For the stronger diffusive hydrogel $\mu_s = 10$ cm^{-1}, the transmitted intensity through the sample is 6 times weaker than in previous case. This decreases the SNR to ≈ 1.6. Fourier components are here again fetched without averaging, and the modulus
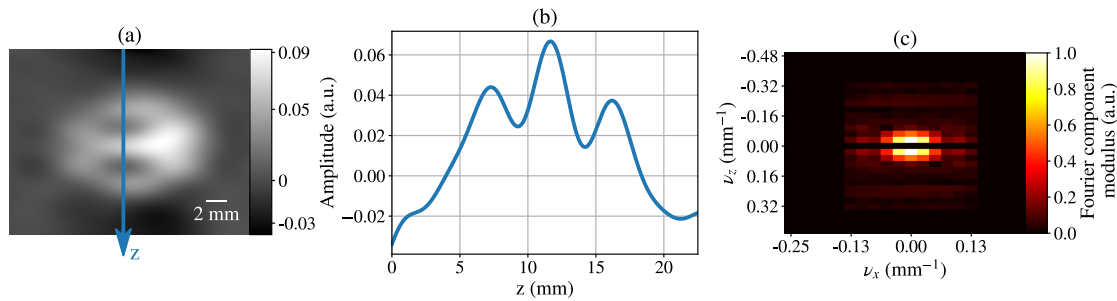
Fig. 6. FT-AOI of two ink inclusions buried within a 1-cm-thick scattering hydrogel with a reduced scattering coefficient of 1 cm^{-1}. (a) The image is obtained by gathering the 110 experimentally measured Fourier components for $-5 \leq m \leq 5$ and $1 \leq n \leq 10$. (b) The profile is drawn following the blue line on the acousto-optic image crossing the two dark spots. (c) Modulus of the four-phase acquired Fourier components.

Fig. 7. FT-AO images of two ink inclusions embedded in 1-cm-thick scattering hydrogel with a reduced scattering coefficient of 10 cm^{-1}. (a) The image is obtained by gathering the 110 experimentally measured Fourier components for $-5 \leq m \leq 5$ and $1 \leq n \leq 10$. (b) The profile is drawn following the blue line on the acousto-optic image crossing the two dark spots. (c) Modulus of the four-phase acquired Fourier components.
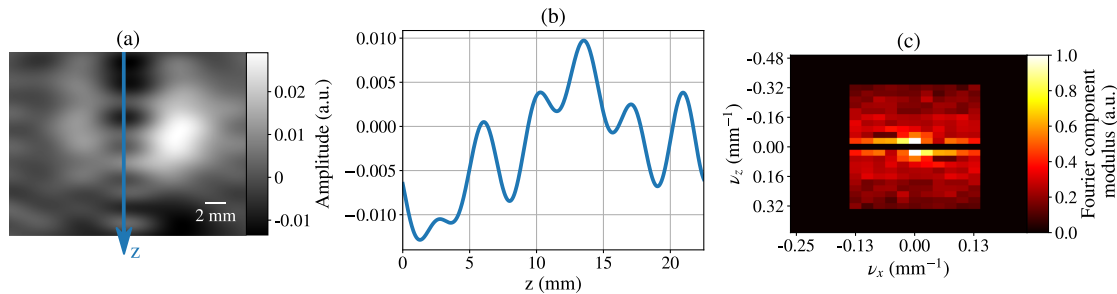
of the noisy Fourier components is shown in Fig. 7(c). The two inclusions are still discriminated. The noise, however, affects the image reconstruction, as we see in Figs. 7(a) and 7(b). We observe a phase offset between high- and low-frequency components such that several inclusions of different sizes seem to appear, which shows the limitation of the method at low SNR. We nevertheless emphasize that this result is obtained without averaging, thereby demonstrating the robustness of our imaging strategy.

4. CONCLUSION

In conclusion, we have shown that the FT-AOI combined with an off-axis detection can achieve averaging-free imaging over a 3×3 cm^2 field of view with millimeter resolution. This camera-based detection integrates the energy of multiple speckle grains impinging on the detector. A reference beam is used to extract and demodulate the tagged signal, and as a result of autocorrelation, only photons allowed by the tagging function are detected. This allows one to perform imaging in the Fourier domain of the object while still tagging a large volume inside the sample. The camera integration time is kept below a millisecond so as to be insensitive to speckle decorrelation. In addition, the overall acquisition time of an image was 1.5 s, making this method adapted for *in vivo* monitoring.

This short acquisition time is only possible because of the large volume of tagged photon inherent to the method, even with limited effective collection on the camera and low pressure peak powers. We plan to further increase the image SNR by using the full camera chip along with GPU stream analysis.

In this article, image reconstruction was performed using a straightforward two-dimensional iFT. In the future, we plan to investigate other reconstruction strategies, in particular one that can account for diffraction effects visible on the tagging function. This can be done, for instance, by measuring an acousto-optic tagging matrix, thereby opening the way to a wide variety of tagging strategies for optimal imaging.

Disclosures. The authors declare no conflicts of interest.

Data Availability. Data underlying the results presented in this paper are not publicly available at this time but may be obtained from the authors upon reasonable request.

Supplemental document. See Supplement 1 for supporting content.

REFERENCES

1. W.-F. Cheong, S. A. Prahl, and A. J. Welch, "A review of the optical properties of biological tissues," IEEE J. Quantum Electron. **26**, 2166–2185 (1990).
2. D. Huang, E. A. Swanson, C. P. Lin, J. S. Schuman, W. G. Stinson, W. Chang, M. R. Hee, T. Flotte, K. Gregory, C. A. Puliafito, and J. G. Fujimoto, "Optical coherence tomography," Science **254**, 1178–1181 (1991).
3. W. Drexler and J. G. Fujimoto, *Optical Coherence Tomography: Technology and Applications* (Springer, 2008).
4. A. Badon, D. Li, G. Lerosey, A. C. Boccara, M. Fink, and A. Aubry, "Smart optical coherence tomography for ultra-deep imaging through highly scattering media," Sci. Adv. **2**, e1600370 (2016).

5. D. A. Boas, D. H. Brooks, E. L. Miller, C. A. DiMarzio, M. Kilmer, R. J. Gaudette, and Q. Zhang, "Imaging the body with diffuse optical tomography," IEEE Signal Process. Mag. **18**(6), 57–75 (2001).

6. S. R. Arridge and W. R. B. Lionheart, "Nonuniqueness in diffusion-based optical tomography," Opt. Lett. **23**, 882–884 (1998).

7. B. Brendel and T. Nielsen, "Selection of optimal wavelengths for spectral reconstruction in diffuse optical tomography," J. Biomed. Opt. **14**, 034041 (2009).

8. M. Xu and L. V. Wang, "Photoacoustic imaging in biomedicine," Rev. Sci. Instrum. **77**, 041101 (2006).

9. H. F. Zhang, K. Maslov, G. Stoica, and L. V. Wang, "Functional photo-acoustic microscopy for high-resolution and noninvasive in vivo imaging," Nat. Biotechnol. **24**, 848–851 (2006).

10. E. Bossy, K. Daoudi, A.-C. Boccara, M. Tanter, J.-F. Aubry, G. Montaldo, and M. Fink, "Time reversal of photoacoustic waves," Appl. Phys. Lett. **89**, 184108 (2006).

11. L. V. Wang and S. Hu, "Photoacoustic tomography: in vivo imaging from organelles to organs," Science **335**, 1458–1462 (2012).

12. T. Chaigne, O. Katz, A. C. Boccara, M. Fink, E. Bossy, and S. Gigan, "Controlling light in scattering media non-invasively using the photo-acoustic transmission matrix," Nat. Photonics **8**, 58–64 (2014).

13. J. Gunther and S. Andersson-Engels, "Review of current methods of acousto-optical tomography for biomedical applications," Front. Optoelectron. **10**, 211 (2017).

14. A. Bengtsson, D. Hill, M. Li, M. Di, M. Cinthio, T. Erlöv, S. Andersson-Engels, N. Reistad, A. Walther, L. Rippe, and S. Kröll, "Characterization and modeling of acousto-optic signal strengths in highly scattering media," Biomed. Opt. Express **10**, 5565–5584 (2019).

15. W. Leutz and G. Maret, "Ultrasonic modulation of multiply scattered light," Physica B (Amsterdam) **204**, 14–19 (1995).

16. M. Gross, P. Goy, B. Forget, M. Atlan, F. Ramaz, A. Boccara, and A. Dunn, "Heterodyne detection of multiply scattered monochromatic light with a multipixel detector," Opt. Lett. **30**, 1357–1359 (2005).

17. A. Lev and B. Sfez, "In vivo demonstration of the ultrasound-modulated light technique," J. Opt. Soc. Am. A **20**, 2347–2354 (2003).

18. Y. Liu, P. Lai, C. Ma, X. Xu, A. A. Grabar, and L. V. Wang, "Optical focusing deep inside dynamic scattering media with near-infrared time-reversed ultrasonically encoded (TRUE) light," Nat. Commun. **6**, 5904 (2015).

19. M. M. Qureshi, J. Brake, H.-J. Jeon, H. Ruan, Y. Liu, A. M. Safi, T. J. Eom, C. Yang, and E. Chung, "In vivo study of optical speckle decorrelation time across depths in the mouse brain," Biomed. Opt. Express **8**, 4855–4864 (2017).

20. F. Ramaz, B. Forget, M. Atlan, A.-C. Boccara, M. Gross, P. Delaye, and G. Roosen, "Photorefractive detection of tagged photons in ultrasound modulated optical tomography of thick biological tissues," Opt. Express **12**, 5469–5474 (2004).

21. C. Venet, M. Bocoum, J.-B. Laudereau, T. Chaneliere, F. Ramaz, and A. Louchet-Chauvet, "Ultrasound-modulated optical tomography in scattering media: flux filtering based on persistent spectral hole burning in the optical diagnosis window," Opt. Lett. **43**, 3993–3996 (2018).

22. E. Benoit a La Guillaume, S. Farahi, E. Bossy, M. Gross, and F. Ramaz, "Acousto-optical coherence tomography with a digital holographic detection scheme," Opt. Lett. **37**, 3216–3218 (2012).

23. M. Gross, P. Goy, and M. Al-Koussa, "Shot-noise detection of ultrasound-tagged photons in ultrasound-modulated optical imaging," Opt. Lett. **28**, 2482–2484 (2003).

24. M. Kronrod, N. Merzlyakov, and L. Yaroslavskii, "Reconstruction of a hologram with a computer," Sov. Phys. Tech. Phys. **17**, 333 (1972).

25. L. Onural and P. D. Scott, "Digital decoding of in-line holograms," Opt. Eng. **26**, 261124 (1987).

26. M. Bocoum, J.-L. Gennisson, J.-B. Laudereau, A. Louchet-Chauvet, J.-M. Tualle, and F. Ramaz, "Structured ultrasound-modulated optical tomography," Appl. Opt. **58**, 1933–1940 (2019).

27. F. A. Marks, H. W. Tomlinson, and G. W. Brooksby, "Comprehensive approach to breast cancer detection using light: photon localization by ultrasound modulation and tissue characterization by spectral discrimination," Proc. SPIE **1888**, 500–511 (1993).

28. B.-C. Forget, F. Ramaz, M. Atlan, J. Selb, and A.-C. Boccara, "High-contrast fast Fourier transform acousto-optical tomography of phantom tissues with a frequency-chirp modulation of the ultrasound," Appl. Opt. **42**, 1379–1383 (2003).

29. M. Lesaffre, S. Farahi, M. Gross, P. Delaye, C. Boccara, and F. Ramaz, "Acousto-optical coherence tomography using random phase jumps on ultrasound and light," Opt. Express **17**, 18211–18218 (2009).

30. K. Barjean, F. Ramaz, and J.-M. Tualle, "Theoretical study of Fourier-transform acousto-optic imaging," J. Opt. Soc. Am. A **33**, 854–862 (2016).

31. K. Barjean, K. Contreras, J.-B. Laudereau, É. Tinet, D. Ettori, F. Ramaz, and J.-M. Tualle, "Fourier transform acousto-optic imaging with a custom-designed CMOS smart-pixels array," Opt. Lett. **40**, 705–708 (2015).

32. M. Bocoum, J.-L. Gennisson, A. A. Grabar, F. Ramaz, and J.-M. Tualle, "Reconstruction of bi-dimensional images in Fourier-transform acousto-optic imaging," Opt. Lett. **45**, 4855–4858 (2020).

33. J. A. Jensen, "Simulation of advanced ultrasound systems using field ii," in *2nd IEEE International Symposium on Biomedical Imaging: Nano to Macro (IEEE Cat No. 04EX821)* (IEEE, 2004), pp. 636–639.

34. S. L. Jacques, "Optical properties of biological tissues: a review," Phys. Med. Biol. **58**, R37–R61 (2013).

35. T. Hall, M. Bilgen, M. Insana, and T. Krouskop, "Phantom materials for elastography," IEEE Trans. Ultrason. Ferroelectr. Freq. Control **44**, 1355–1365 (1997).

36. H. J. van Staveren, C. J. M. Moes, J. van Marie, and S. A. Prahl, "Light scattering in Intralipid-10% in the wavelength range of 400-1 100 nm," Appl. Opt. **30**, 4507–4514 (1991).

37. R. Phillips and G. Harris, "Information for manufacturers seeking marketing clearance of diagnostic ultrasound systems and transducers," Tech. Rep. (Food and Drug Administration, 2008).